



Cite this: *RSC Adv.*, 2019, 9, 592

# Suppression of GeO<sub>x</sub> interfacial layer and enhancement of the electrical performance of the high-*K* gate stack by the atomic-layer-deposited AlN buffer layer on Ge metal-oxide-semiconductor devices

Chin-I. Wang,<sup>a</sup> Teng-Jan Chang,<sup>a</sup> Chun-Yuan Wang,<sup>a</sup> Yu-Tung Yin,<sup>a</sup> Jing-Jong Shyue,<sup>b</sup> Hsin-Chih Lin<sup>a</sup> and Miin-Jang Chen<sup>\*a</sup>

For high-performance nanoscale Ge-based transistors, one important point of focus is interfacial germanium oxide (GeO<sub>x</sub>), which is thermodynamically unstable and easily desorbed. In this study, an atomic-layer-deposited AlN buffer layer was introduced between the crystalline ZrO<sub>2</sub> high-*K* gate dielectrics and epitaxial Ge, in order to reduce the formation of interfacial GeO<sub>x</sub>. The results of X-ray photoelectron spectroscopy and high-resolution transmission electron microscopy demonstrate that the AlN buffer layer suppressed the formation of interfacial GeO<sub>x</sub>. Hence, significant enhancement of the electrical characteristics of Ge metal-oxide-semiconductor (MOS) capacitors was achieved with a two-orders-of-magnitude reduction in the gate leakage current, a 34% enhancement of the MOS capacitance, and a lower interfacial state density. The results indicate that the AlN buffer layer is effective in providing a high-quality interface to improve the electrical performance of advanced Ge MOS devices.

Received 14th September 2018  
 Accepted 3rd December 2018

DOI: 10.1039/c8ra07652a

[rsc.li/rsc-advances](http://rsc.li/rsc-advances)

## 1. Introduction

Over the last decade, it has become increasingly difficult to improve the performance of silicon (Si) metal-oxide-semiconductor (MOS) field-effect transistors (FETs) *via* conventional device scaling. Due to high carrier mobility, germanium (Ge) and III-V compound MOSFETs have been regarded as very promising candidates for the further improvement of device performance and scaling.<sup>1–4</sup> However, the lack of high-quality and thermodynamically stable gate dielectrics is a major problem in implementing Ge and III-V semiconductors as the channel materials.<sup>5–10</sup> For Ge, it is difficult to suppress the formation of a low-*K* germanium oxide (GeO<sub>x</sub>) interfacial layer (IL) at the high-*K* and Ge interface, which limits the minimum achievable equivalent oxide thickness.<sup>11,12</sup> In contrast to the SiO<sub>2</sub>/Si system, interfacial GeO<sub>x</sub> has been reported to be thermodynamically unstable.<sup>5</sup> The smaller conduction band offset at the GeO<sub>x</sub>/Ge interface also results in an increase in the gate leakage current.<sup>13</sup> Therefore, it is essential to prevent the formation of interfacial GeO<sub>x</sub> in high-performance Ge-based MOSFETs.<sup>13,14</sup>

Many methods have been used to passivate the defects and achieve a stable high-*K*/Ge interface, such as the use of ultrathin

Si, high-quality Ge oxides, and rare-earth oxides (Y<sub>2</sub>O<sub>3</sub>, SmGeO<sub>x</sub>, *etc.*),<sup>6,15–17</sup> One of the most widely used methods is the insertion of an Al<sub>2</sub>O<sub>3</sub> buffer layer between the high-*K* oxide and Ge because of the high bandgap and good thermal stability of Al<sub>2</sub>O<sub>3</sub>.<sup>18,19</sup> Besides, it has been reported that nitrogen incorporation into GeO<sub>x</sub> yields an improvement in the thermal stability and the dielectric constant.<sup>20,21</sup> However, an unstable GeO<sub>x</sub> is usually formed at the Al<sub>2</sub>O<sub>3</sub>/Ge and Ge-oxynitride/Ge interfaces. Furthermore, the use of germanium nitride (Ge<sub>3</sub>N<sub>4</sub> or GeN<sub>x</sub>) as the gate dielectric and the buffer layer has been demonstrated to exhibit well-behaved capacitance–voltage characteristics.<sup>22–25</sup> This improvement in the electrical performance may be the result of the suppression of interfacial GeO<sub>x</sub> because the preparation of the nitride does not involve the use of oxygen.

AlN is a good material for gate dielectrics and buffer layers because it has a higher dielectric constant than GeO<sub>x</sub>, good chemical stability, and a wide bandgap of ~6.2 eV.<sup>26–28</sup> AlN thin films are conventionally prepared by chemical vapor deposition (CVD) and sputtering.<sup>29,30</sup> However, the typical deposition temperature for AlN prepared using CVD is greater than 700 °C,<sup>31</sup> which is unfavorable for the integration of semiconductor processing. Besides, it is difficult to deposit high-quality nanoscale thin films using sputtering.<sup>32</sup> Recently, atomic layer deposition (ALD) has been reported for the preparation of high-quality nanoscale AlN thin films at low temperatures.<sup>26,31</sup> In this paper, remote plasma ALD (RP-ALD) was used to deposit a nanoscale AlN buffer layer between the

<sup>a</sup>Department of Materials Science and Engineering, National Taiwan University, Taipei, Taiwan. E-mail: [mjchen@ntu.edu.tw](mailto:mjchen@ntu.edu.tw)

<sup>b</sup>Research Center for Applied Science, Academia Sinica, Taipei, Taiwan



crystalline  $\text{ZrO}_2$  high- $K$  gate dielectrics and Ge. The interfacial  $\text{GeO}_x$  was suppressed by the AlN buffer layer, so the capacitance equivalent thickness (CET), the interfacial state density ( $D_{it}$ ) and the gate leakage current ( $J_g$ ) of Ge MOS capacitors were significantly improved.

## 2. Experiments

The gate stacks in MOS capacitors are plotted schematically in Fig. 1. A Ge epitaxial layer was grown by remote plasma chemical vapor deposition using  $\text{GeH}_4$  at 375 °C on a highly-doped (0.001–0.003  $\Omega$  cm)  $n$ -type Si substrate. After pre-cleaning, the samples were immersed in dilute HF (1 min) and then rinsed with de-ionized water (30 s) for several cycles, in order to remove the native oxide on the Ge. The gate stacks, which were composed of  $\text{ZrO}_2$ ,  $\text{Al}_2\text{O}_3/\text{ZrO}_2$ , and AlN/ $\text{ZrO}_2$ , were then immediately deposited by RP-ALD (Fiji, Ultratech) at 250 °C. Tetrakis(dimethylamino)zirconium (TDMAZ), trimethylaluminum (TMA),  $\text{O}_2$  plasma, and  $\text{N}_2/\text{H}_2$  plasma were respectively used as the precursors and reactants for Zr, Al, O, and N. A platinum (Pt) top electrode with an area of  $3 \times 10^{-4}$   $\text{cm}^2$  was deposited by radio-frequency sputtering, and then an aluminum (Al) back contact was then produced by thermal evaporation. Finally, all samples were annealed in a furnace at 450 °C in  $\text{N}_2$  ambient for 30 minutes.

The chemical bonding in the gate stacks was determined by X-ray photoelectron spectroscopy (XPS) using Al  $K\alpha$  radiation at 1486.6 eV. The cross-sectional images of the gate stacks were observed using high-resolution transmission electron microscopy (HRTEM, Philips Tecnai F20 G2 FEI-TEM, 200 kV). The crystalline phases of  $\text{ZrO}_2$  were measured by grazing incident angle X-ray diffraction (GIXRD) using Cu  $K\alpha$  radiation at an incident angle of 0.5°. The capacitance density *versus* voltage ( $C$ - $V$ ), the leakage current density *versus* voltage ( $I$ - $V$ ), and the conductance density *versus* the frequency ( $G$ - $f$ ) curves of the gate stacks were characterized using an Agilent B1500A semiconductor device analyzer at room temperature.

## 3. Results and discussions

Fig. 2 shows the Ge 3d XPS spectra of the  $\text{ZrO}_2$ ,  $\text{Al}_2\text{O}_3/\text{ZrO}_2$ , and AlN/ $\text{ZrO}_2$  gate stacks with and without the annealing treatment, which reveals the oxidation states of Ge. The XPS spectra can be decomposed into the peaks corresponding to the binding

energies at 29.4 eV (Ge), 31.7 eV (GeO), 33.6 eV ( $\text{GeO}_2$ ), and 30.9 eV (Ge-N).<sup>19</sup> The XPS spectra of the samples without the annealing treatment are shown in Fig. 2(a)–(c). The presence of the GeO oxidation state in the  $\text{ZrO}_2$  sample (Fig. 2(a)) is attributed to the supply of oxygen from  $\text{ZrO}_2$ . Fig. 2(b) reveals that the interfacial GeO was suppressed in the  $\text{Al}_2\text{O}_3/\text{ZrO}_2$  gate stack compared to that in the  $\text{ZrO}_2$  sample, which can be deduced from the lower Gibbs free energy of  $\text{Al}_2\text{O}_3$  than that of  $\text{ZrO}_2$ .<sup>33</sup> It can be seen in Fig. 2(c) that the AlN buffer layer led to the formation of Ge–N bonds, and the GeO oxidation states were almost absent in the AlN/ $\text{ZrO}_2$  sample because oxygen was not involved during AlN deposition. The result also suggests that the diffusion of oxygen from  $\text{ZrO}_2$  toward the interface was effectively blocked by the AlN buffer layer, and so the formation of interfacial  $\text{GeO}_x$  was suppressed. Moreover, Fig. 2(d)–(f) are the XPS spectra of the samples treated with the annealing process. As compared with Fig. 2(a) and (b), the annealing treatment gave rise to an increase in the GeO signals and the formation of  $\text{GeO}_2$  oxidation states in the  $\text{ZrO}_2$  and  $\text{Al}_2\text{O}_3/\text{ZrO}_2$  gate stacks:<sup>34</sup>



The decomposition of GeO into  $\text{GeO}_2$  and Ge is ascribed to the lower Gibbs free energy of  $\text{GeO}_2$  than that of GeO.<sup>34</sup> The outcome indicates that the annealing process facilitated the formation of interfacial  $\text{GeO}_x$ . Notice that no obvious interfacial  $\text{GeO}_x$  appeared in the XPS spectrum of the AlN/ $\text{ZrO}_2$  gate stack as shown in Fig. 2(f). The result confirms again that the AlN buffer layer could effectively restrain oxygen diffusion during the  $\text{ZrO}_2$  deposition and annealing processes.

The Al 2p XPS spectra of the  $\text{Al}_2\text{O}_3/\text{ZrO}_2$  and AlN/ $\text{ZrO}_2$  gate stacks are shown in Fig. 3. The Al–O bond (75.6 eV) was present in the  $\text{Al}_2\text{O}_3/\text{ZrO}_2$  sample due to the introduction of the  $\text{Al}_2\text{O}_3$  buffer layer. The Al 2p peak of the AlN/ $\text{ZrO}_2$  sample was located near 74.6 eV, which is associated with the Al–N bond because AlN was substituted for the  $\text{Al}_2\text{O}_3$  buffer layer.<sup>35</sup> Depositing  $\text{ZrO}_2$  on the AlN buffer layer results in a slight shift in the Al 2p peak ( $\sim 75$  eV) from the standard Al–N bond at 74.6 eV toward the Al–O bond at 75.6 eV, indicating the partial oxidation of AlN.

The HRTEM images of the  $\text{ZrO}_2$ ,  $\text{Al}_2\text{O}_3/\text{ZrO}_2$ , and AlN/ $\text{ZrO}_2$  gate stacks are shown in Fig. 4. It is seen that the total physical thickness of all the samples was approximately 7.5 nm. The  $\text{ZrO}_2$  layer featured a crystalline lattice in the images for all of the samples, which demonstrates that  $\text{ZrO}_2$  was crystallized

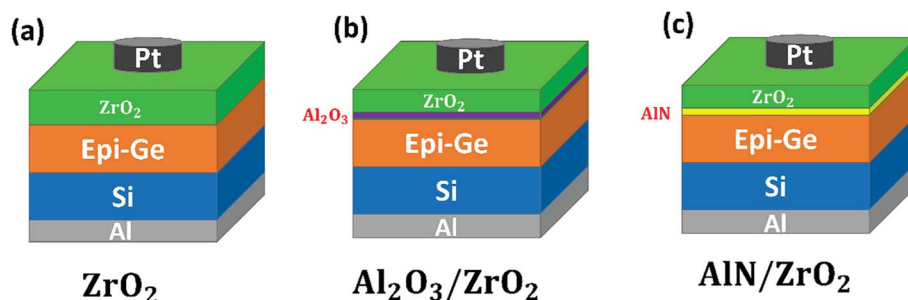


Fig. 1 Schematic of the (a)  $\text{ZrO}_2$ , (b)  $\text{Al}_2\text{O}_3/\text{ZrO}_2$ , and (c) AlN/ $\text{ZrO}_2$  gate stacks.



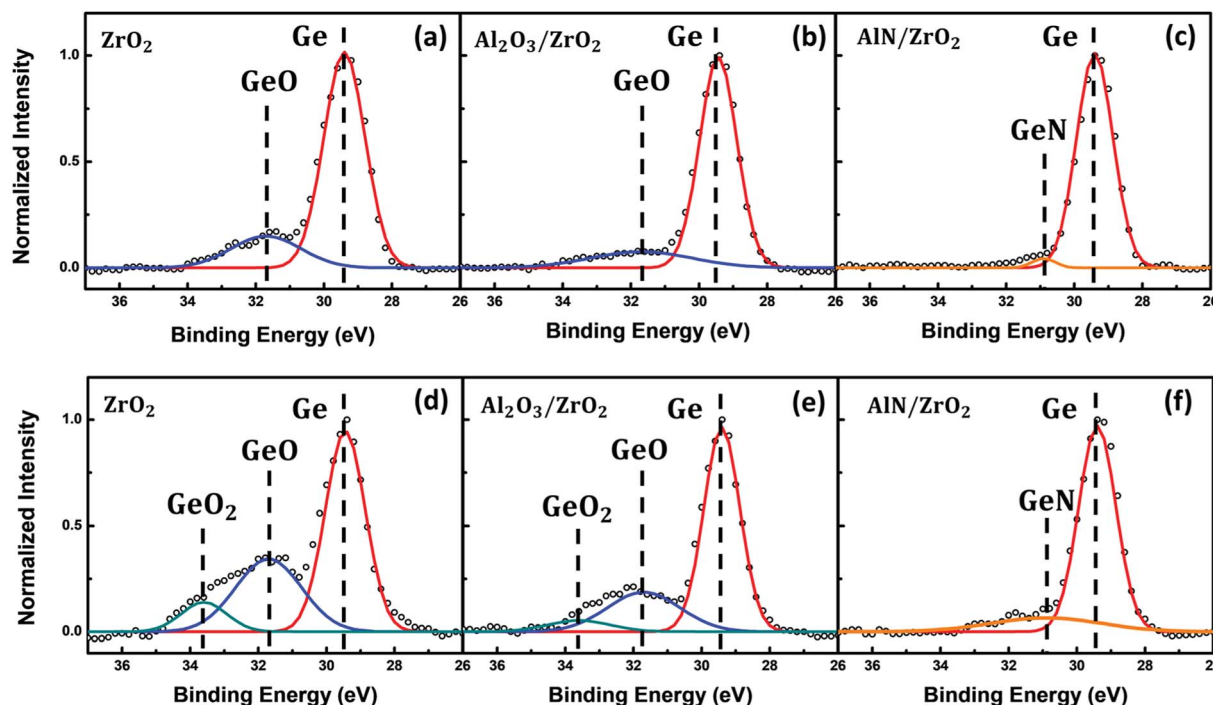


Fig. 2 The Ge 3d XPS spectra of the (a)  $\text{ZrO}_2$ , (b)  $\text{Al}_2\text{O}_3/\text{ZrO}_2$ , and (c)  $\text{AlN}/\text{ZrO}_2$  gate stacks without the annealing treatment and the (d)  $\text{ZrO}_2$ , (e)  $\text{Al}_2\text{O}_3/\text{ZrO}_2$ , and (f)  $\text{AlN}/\text{ZrO}_2$  gate stacks treated with the annealing process (in a furnace at  $450\text{ }^\circ\text{C}$  for 30 minutes in  $\text{N}_2$  ambient). The intensity of the Ge peak of each sample was normalized to one. The annealing treatment facilitated the formation of interfacial  $\text{GeO}_x$  in the  $\text{ZrO}_2$  and  $\text{Al}_2\text{O}_3/\text{ZrO}_2$  gate stacks. The interfacial  $\text{GeO}_x$  was significantly suppressed in the  $\text{AlN}/\text{ZrO}_2$  gate stack.

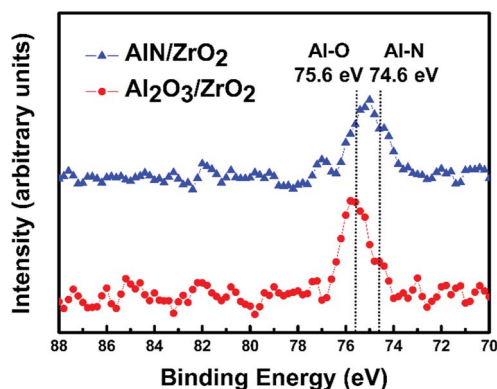


Fig. 3 Al 2p XPS spectra of the  $\text{Al}_2\text{O}_3/\text{ZrO}_2$  and  $\text{AlN}/\text{ZrO}_2$  gate stacks. The Al–O (75.6 eV) and Al–N (74.6 eV) bonds were present in the  $\text{Al}_2\text{O}_3/\text{ZrO}_2$  and  $\text{AlN}/\text{ZrO}_2$  samples.

during thermal annealing.<sup>36</sup> In Fig. 4(a), there is an obvious and rough interfacial  $\text{GeO}_x$  layer in the  $\text{ZrO}_2$  sample. An  $\text{Al}_2\text{O}_3$  buffer layer and interfacial  $\text{GeO}_x$  are observed in the  $\text{Al}_2\text{O}_3/\text{ZrO}_2$  gate stack as shown in Fig. 4(b). Fig. 4(c) reveals a sharp interface without interfacial  $\text{GeO}_x$  between  $\text{AlN}$  and  $\text{Ge}$ , indicating that the  $\text{AlN}$  buffer layer was capable of suppressing interfacial  $\text{GeO}_x$ . The HRTEM results are in good agreement with the Ge 3d XPS spectra shown in Fig. 2.

The GIXRD patterns of the  $\text{ZrO}_2$ ,  $\text{Al}_2\text{O}_3/\text{ZrO}_2$ , and  $\text{AlN}/\text{ZrO}_2$  gate stacks are shown in Fig. 5. There is an obvious diffraction peak at  $2\theta = 30.4^\circ$  in all of the samples, which corresponds to

the tetragonal (101) phase (88-1007 JCPDS) or the cubic (111) phase (49-1642 JCPDS) of  $\text{ZrO}_2$ .<sup>37</sup> The tetragonal/cubic phase in  $\text{ZrO}_2$  had a much higher dielectric constant than amorphous  $\text{ZrO}_2$ , which allows further CET scaling.<sup>38</sup> Although tetragonal/cubic  $\text{ZrO}_2$  was thermodynamically stable at temperatures greater than  $1170\text{ }^\circ\text{C}$ ,<sup>39,40</sup> the tetragonal/cubic phase had been observed in nanoscale  $\text{ZrO}_2$  thin films.<sup>41</sup> The presence of tetragonal/cubic  $\text{ZrO}_2$  in the nanoscale layers, as shown in Fig. 5, is consistent with the results of previous studies.<sup>36,41</sup>

The  $C$ - $V$  curves of the  $\text{ZrO}_2$ ,  $\text{Al}_2\text{O}_3/\text{ZrO}_2$ , and  $\text{AlN}/\text{ZrO}_2$  gate stacks are shown in Fig. 6(a). The capacitance of the  $\text{AlN}/\text{ZrO}_2$  sample was much greater than that of the  $\text{ZrO}_2$  and  $\text{Al}_2\text{O}_3/\text{ZrO}_2$  samples. Table 1 shows the CET and the effective dielectric constant ( $k_{\text{eff}}$ ) of the  $\text{ZrO}_2$ ,  $\text{Al}_2\text{O}_3/\text{ZrO}_2$ , and  $\text{AlN}/\text{ZrO}_2$  gate stacks. These values were derived from the  $C$ - $V$  curves. The CET and  $k_{\text{eff}}$  values of the  $\text{ZrO}_2$  sample are 2.35 nm and 12.42, respectively. The  $k_{\text{eff}}$  of the  $\text{ZrO}_2$  sample is much lower than the dielectric constant of tetragonal/cubic  $\text{ZrO}_2$ ,<sup>42,43</sup> which can be deduced from the presence of low- $K$  interfacial  $\text{GeO}_x$  in the  $\text{ZrO}_2$  sample, as shown in the XPS spectrum and the HRTEM image (Fig. 2(d) and 4(a)). Although the low- $K$  interfacial  $\text{GeO}_x$  was suppressed by the  $\text{Al}_2\text{O}_3$  buffer layer, as demonstrated by the XPS spectrum (Fig. 2(e)), the introduction of the  $\text{Al}_2\text{O}_3$  buffer layer between  $\text{ZrO}_2$  and  $\text{Ge}$  still caused a slight degradation of the CET (2.38 nm) and  $k_{\text{eff}}$  (12.29) of the  $\text{Al}_2\text{O}_3/\text{ZrO}_2$  gate stack because  $\text{Al}_2\text{O}_3$  has a lower dielectric constant than  $\text{ZrO}_2$ . The substitution of  $\text{AlN}$  for  $\text{Al}_2\text{O}_3$  as the buffer layer led to a significant decrease in the CET (1.75 nm) and an increase in the  $k_{\text{eff}}$



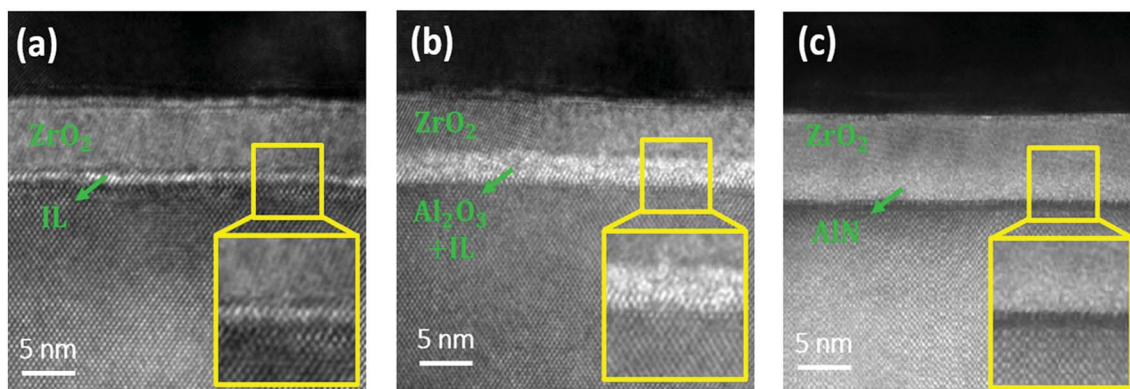


Fig. 4 Cross-sectional HRTEM images of the (a)  $\text{ZrO}_2$ , (b)  $\text{Al}_2\text{O}_3/\text{ZrO}_2$ , and (c)  $\text{AlN}/\text{ZrO}_2$  gate stacks. There is a sharp interface between  $\text{AlN}$  and  $\text{Ge}$  in the  $\text{AlN}/\text{ZrO}_2$  sample.

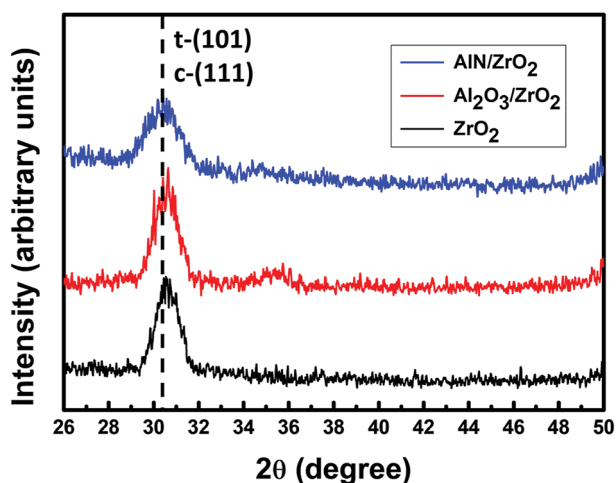


Fig. 5 GIXRD patterns of  $\text{ZrO}_2$ ,  $\text{Al}_2\text{O}_3/\text{ZrO}_2$ , and  $\text{AlN}/\text{ZrO}_2$  gate stacks. The obvious diffraction peak at  $2\theta = 30.4^\circ$  is associated with tetragonal/cubic  $\text{ZrO}_2$ .

(16.72) of the  $\text{AlN}/\text{ZrO}_2$  sample, which is mainly attributed to the suppression of the interfacial  $\text{GeO}_x$ , as clearly shown in Fig. 2(f) and 4(c).

Fig. 6(b) and Table 1 show the  $I$ - $V$  curves and the  $J_g$  of the  $\text{ZrO}_2$ ,  $\text{Al}_2\text{O}_3/\text{ZrO}_2$ , and  $\text{AlN}/\text{ZrO}_2$  gate stacks. The  $\text{ZrO}_2$  sample had a high  $J_g$  value of  $1.82 \times 10^{-1} \text{ A cm}^{-2}$  as a result of the leakage current path *via* the grain boundaries in crystalline  $\text{ZrO}_2$ . Due to the high bandgap of  $\text{Al}_2\text{O}_3$ , the presence of the  $\text{Al}_2\text{O}_3$  buffer layer resulted in a decrease in the  $J_g$  ( $2.60 \times 10^{-2} \text{ A cm}^{-2}$ ) of the  $\text{Al}_2\text{O}_3/\text{ZrO}_2$  sample. There was a significant reduction in the  $J_g$  ( $1.12 \times 10^{-3} \text{ A cm}^{-2}$ ) of the  $\text{AlN}/\text{ZrO}_2$  gate stack, which is two orders of magnitude lower than that of the  $\text{ZrO}_2$  sample because of the insertion of the  $\text{AlN}$  buffer layer. This can be understood from the suppressed growth of interfacial  $\text{GeO}_x$ , which has a low conduction band offset of only  $\sim 0.8 \text{ eV}$ .<sup>44</sup>

The  $D_{it}$  value was measured by the conductance (Nicollian-Goetzberger) method.<sup>45,46</sup> Fig. 7(a) shows the equivalent parallel conductance over the angular frequency ( $G_p/\omega$ ) as a function of the frequency of the  $\text{ZrO}_2$ ,  $\text{Al}_2\text{O}_3/\text{ZrO}_2$ , and  $\text{AlN}/\text{ZrO}_2$  gate stacks. The value of  $D_{it}$  was estimated from the maximum value of  $G_p/\omega$  as:<sup>45</sup>

$$D_{it} = \frac{2.5}{Aq} \left( \frac{G_p}{\omega} \right)_{\max}$$

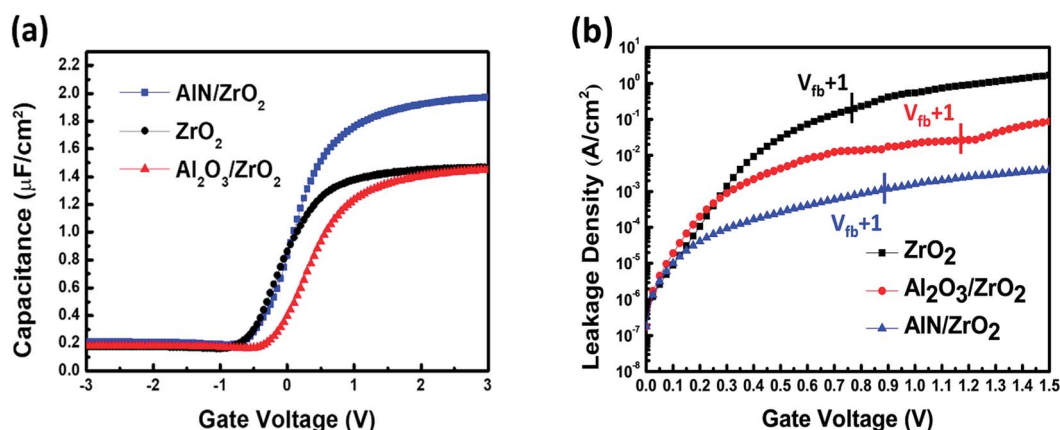


Fig. 6 (a)  $C$ - $V$  and (b)  $I$ - $V$  characteristics of the  $\text{ZrO}_2$ ,  $\text{Al}_2\text{O}_3/\text{ZrO}_2$ , and  $\text{AlN}/\text{ZrO}_2$  gate stacks. The  $\text{AlN}/\text{ZrO}_2$  gate stack had a higher capacitance and a lower  $J_g$  than the  $\text{ZrO}_2$  or  $\text{Al}_2\text{O}_3/\text{ZrO}_2$  samples.



**Table 1** The capacitance equivalent thickness (CET), the effective dielectric constant ( $k_{\text{eff}}$ ), the gate leakage current ( $J_g$ ), and the interfacial state density ( $D_{\text{it}}$ ) of the  $\text{ZrO}_2$ ,  $\text{Al}_2\text{O}_3/\text{ZrO}_2$ , and  $\text{AlN}/\text{ZrO}_2$  gate stacks<sup>a</sup>

Sample	CET (nm)	$k_{\text{eff}}$	$J_g$ ( $\text{A cm}^{-2}$ )	$D_{\text{it}}$ ( $\text{cm}^{-2} \text{eV}^{-1}$ )
$\text{ZrO}_2$	2.35	12.42	$1.82 \times 10^{-1}$	$9.08 \times 10^{12}$
$\text{Al}_2\text{O}_3/\text{ZrO}_2$	2.38	12.29	$2.60 \times 10^{-2}$	$6.46 \times 10^{12}$
$\text{AlN}/\text{ZrO}_2$	1.75	16.72	$1.12 \times 10^{-3}$	$3.85 \times 10^{12}$

<sup>a</sup> These values were extracted from the  $C$ - $V$ ,  $I$ - $V$ , and  $G$ - $f$  curves as shown in Fig. 6 and 7. The leakage current density  $J_g$  was determined at  $V_{\text{fb}}$  (flat-band voltage) +1 V. The  $\text{AlN}/\text{ZrO}_2$  gate stack exhibited a significant improvement in CET,  $k_{\text{eff}}$ ,  $J_g$ , and  $D_{\text{it}}$  over the  $\text{ZrO}_2$  and  $\text{Al}_2\text{O}_3/\text{ZrO}_2$  samples.

where  $A$  is the area of the MOS capacitors. The  $D_{\text{it}}$  distributions in the bandgap of the  $\text{ZrO}_2$ ,  $\text{Al}_2\text{O}_3/\text{ZrO}_2$ , and  $\text{AlN}/\text{ZrO}_2$  gate stacks are shown in Fig. 7(b). Since the weak inversion response results in the overestimation of  $D_{\text{it}}$  for Ge at room temperature,<sup>47</sup> the minimum  $D_{\text{it}}$  values near the mid-gap were adopted to characterize the interfacial quality of the  $\text{ZrO}_2$ ,  $\text{Al}_2\text{O}_3/\text{ZrO}_2$ , and  $\text{AlN}/\text{ZrO}_2$  gate stacks.<sup>48</sup> As shown in Table 1, the minimum

$D_{\text{it}}$  of the  $\text{ZrO}_2$ ,  $\text{Al}_2\text{O}_3/\text{ZrO}_2$ , and  $\text{AlN}/\text{ZrO}_2$  samples were  $9.08 \times 10^{12} \text{ cm}^{-2} \text{eV}^{-1}$ ,  $6.46 \times 10^{12} \text{ cm}^{-2} \text{eV}^{-1}$ , and  $3.85 \times 10^{12} \text{ cm}^{-2} \text{eV}^{-1}$ , respectively. Owing to the high thermal stability of the  $\text{Al}_2\text{O}_3$  buffer layer and the reduced growth of interfacial  $\text{GeO}_x$ , the  $D_{\text{it}}$  of the  $\text{Al}_2\text{O}_3/\text{ZrO}_2$  gate stack was lower than that of the  $\text{ZrO}_2$  sample. The introduction of the  $\text{AlN}$  buffer layer caused a further decrease in  $D_{\text{it}}$  of the  $\text{AlN}/\text{ZrO}_2$  gate stack, which is ascribed to the suppression of interfacial  $\text{GeO}_x$  by the  $\text{AlN}$  buffer layer. Because remote  $\text{N}_2/\text{H}_2$  plasma was used as the reactant in the deposition of the  $\text{AlN}$  buffer layer, hydrogen passivation of the interfacial states also led to decrease in  $D_{\text{it}}$  of the  $\text{AlN}/\text{ZrO}_2$  sample.<sup>49</sup>

The  $C$ - $V$  curves of the  $\text{ZrO}_2$ ,  $\text{Al}_2\text{O}_3/\text{ZrO}_2$ , and  $\text{AlN}/\text{ZrO}_2$  gate stacks at various frequencies are shown in Fig. 8. In the frequency range from 1 kHz to 100 kHz, the frequency dispersion is 4.2%, 2.2%, and 1.4% for the  $\text{ZrO}_2$ ,  $\text{Al}_2\text{O}_3/\text{ZrO}_2$ , and  $\text{AlN}/\text{ZrO}_2$  gate stacks at an accumulation bias of 2 V. The larger capacitance at a high frequency of 1 MHz was deduced from the parasitic inductance.<sup>50</sup> The relatively low-frequency dispersion in the  $\text{AlN}/\text{ZrO}_2$  gate stack was correlated with the lower  $D_{\text{it}}$  as compared with the  $\text{ZrO}_2$  and  $\text{Al}_2\text{O}_3/\text{ZrO}_2$  samples.<sup>51</sup>

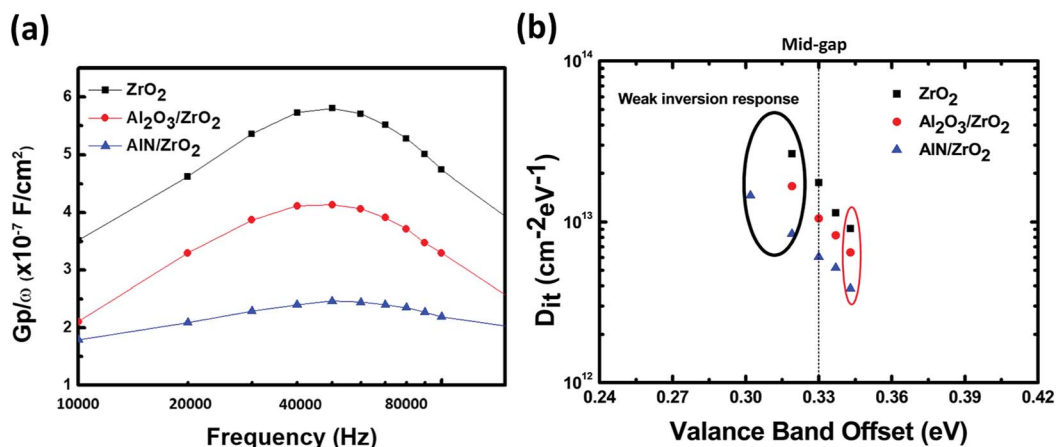


**Fig. 7** (a)  $G_p/\omega$  versus the frequency of the  $\text{ZrO}_2$ ,  $\text{Al}_2\text{O}_3/\text{ZrO}_2$ , and  $\text{AlN}/\text{ZrO}_2$  gate stacks. The  $\text{AlN}/\text{ZrO}_2$  gate stack had the lowest value of  $(G_p/\omega)_{\text{max}}$ , and so the  $D_{\text{it}}$  of the  $\text{AlN}/\text{ZrO}_2$  sample was lower than that of the  $\text{ZrO}_2$  and  $\text{Al}_2\text{O}_3/\text{ZrO}_2$  gate stacks. (b)  $D_{\text{it}}$  distributions versus bandgap energy, which were extracted from the conductance method, of the  $\text{ZrO}_2$ ,  $\text{Al}_2\text{O}_3/\text{ZrO}_2$ , and  $\text{AlN}/\text{ZrO}_2$  gate stacks.

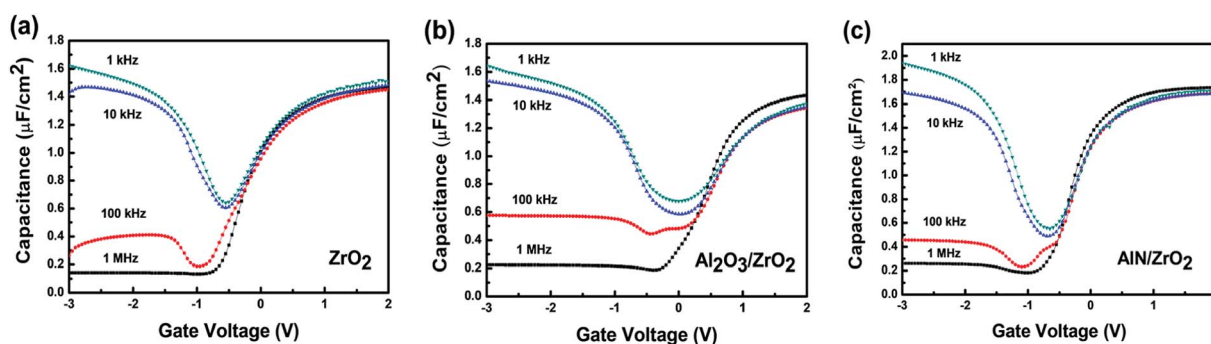


**Fig. 8** The frequency dependence of the  $C$ - $V$  curves of the (a)  $\text{ZrO}_2$ , (b)  $\text{Al}_2\text{O}_3/\text{ZrO}_2$ , and (c)  $\text{AlN}/\text{ZrO}_2$  gate stacks. Low-frequency dispersion was observed in the  $\text{AlN}/\text{ZrO}_2$  sample.



## 4. Conclusion

In this study, the electrical and structural characteristics of the  $\text{ZrO}_2$ ,  $\text{Al}_2\text{O}_3/\text{ZrO}_2$ , and  $\text{AlN}/\text{ZrO}_2$  gate stacks on Ge were investigated carefully. The introduction of an  $\text{Al}_2\text{O}_3$  buffer layer between  $\text{ZrO}_2$  and Ge resulted in a decrease of  $J_g$  value due to the high bandgap of  $\text{Al}_2\text{O}_3$ . However, it is difficult to prevent the growth of unstable, low- $K$  interfacial  $\text{GeO}_x$  using an  $\text{Al}_2\text{O}_3$  buffer layer because oxygen was involved during the deposition of  $\text{Al}_2\text{O}_3$ . The formation of interfacial  $\text{GeO}_x$  was significantly suppressed by an AlN buffer layer, as evidenced by the XPS and HRTEM characterizations. This produced a significant enhancement in the electrical characteristics, including the CET,  $k_{\text{eff}}$ ,  $J_g$ , and  $D_{\text{it}}$  of the AlN/ $\text{ZrO}_2$  gate stack. The results of this study show that an AlN buffer layer is an effective approach to high-quality interfacial engineering for high-performance high- $K$  gate stacks in advanced Ge MOS transistors.

## Conflicts of interest

There are no conflicts to declare.

## Acknowledgements

The authors gratefully acknowledge the financial support of the Taiwan Semiconductor Manufacturing Company (TSMC) and the Ministry of Science and Technology (MOST 107-2622-8-002-018), Taiwan.

## References

- 1 S. Takagi, *et al.*, *IEDM'03 Technical Digest*, IEEE International, 2003, pp. 3.3.1–3.3.4.
- 2 M. V. Fischetti and S. E. Laux, *J. Appl. Phys.*, 1996, **80**(4), 2234–2252.
- 3 K. Saraswat, C. O. Chui, T. Krishnamohan, D. Kim, A. Nayfeh and A. Pethe, *Mater. Sci. Eng., B*, 2006, **135**(3), 242–249.
- 4 S. Takagi, M. Noguchi, M. Kim, S.-H. Kim, C.-Y. Chang, M. Yokoyama, *et al.*, *Solid-State Electron.*, 2016, **125**, 82–102.
- 5 K. Prabhakaran, F. Maeda, Y. Watanabe and T. Ogino, *Appl. Phys. Lett.*, 2000, **76**(16), 2244–2246.
- 6 Y. Seo, T. I. Lee, C. M. Yoon, B.-E. Park, W. S. Hwang, H. Kim, *et al.*, *IEEE Trans. Electron Devices*, 2017, **64**(8), 3303–3307.
- 7 G. He, X. Chen and Z. Sun, *Surf. Sci. Rep.*, 2013, **68**(1), 68–107.
- 8 G. He, J. Gao, H. Chen, J. Cui, Z. Sun and X. Chen, *ACS Appl. Mater. Interfaces*, 2014, **6**(24), 22013–22025.
- 9 G. He, B. Deng, H. Chen, X. Chen, J. Lv, Y. Ma, *et al.*, *APL Mater.*, 2013, **1**(1), 012104.
- 10 G. He, J. Liu, H. Chen, Y. Liu, Z. Sun, X. Chen, *et al.*, *J. Mater. Chem. C*, 2014, **2**(27), 5299–5308.
- 11 Q. Xie, S. Deng, M. Schaekers, D. Lin, M. Caymax, A. Delabie, *et al.*, *Semicond. Sci. Technol.*, 2012, **27**(7), 074012.
- 12 J. Zhang, G. He, L. Zhou, H. Chen, X. Chen, X. Chen, *et al.*, *J. Alloys Compd.*, 2014, **611**, 253–259.
- 13 V. Afanas'ev and A. Stesmans, *Appl. Phys. Lett.*, 2004, **84**(13), 2319–2321.
- 14 Y. Fukuda, K. Kato, H. Toyota, T. Ono, Y. Nagasato and T. Ueno, *Jpn. J. Appl. Phys.*, 2006, **45**(9S), 7351.
- 15 R. Zhang, T. Iwasaki, N. Taoka, M. Takenaka and S. Takagi, *Appl. Phys. Lett.*, 2011, **98**(11), 112902.
- 16 P. Zimmerman, *et al.*, *IEDM'06*, IEEE International, 2006, pp. 1–4.
- 17 C.-C. Lin, Y.-H. Wu, C.-Y. Wu and C.-W. Lee, *IEEE Electron Device Lett.*, 2014, **35**(3), 384–386.
- 18 S. Iwauchi and T. Tanaka, *Jpn. J. Appl. Phys.*, 1971, **10**(2), 260.
- 19 R. Zhang, T. Iwasaki, N. Taoka, M. Takenaka and S. Takagi, *IEEE Trans. Electron Devices*, 2012, **59**(2), 335–341.
- 20 C. O. Chui, F. Ito and K. C. Saraswat, *IEEE Electron Device Lett.*, 2004, **25**(9), 613–615.
- 21 C. O. Chui, F. Ito and K. C. Saraswat, *IEEE Trans. Electron Devices*, 2006, **53**(7), 1501–1508.
- 22 T. Maeda, T. Yasuda, M. Nishizawa, N. Miyata, Y. Morita and S. Takagi, *Appl. Phys. Lett.*, 2004, **85**(15), 3181–3183.
- 23 T. Maeda, M. Nishizawa, Y. Morita and S. Takagi, *Appl. Phys. Lett.*, 2007, **90**(7), 072911.
- 24 Y. Otani, Y. Itayama, T. Tanaka, Y. Fukuda, H. Toyota, T. Ono, *et al.*, *Appl. Phys. Lett.*, 2007, **90**(14), 142114.
- 25 G. V. Rao, M. Kumar, T. Rajesh, D. R. K. Reddy, D. Anjaneyulu, B. Sainath, *et al.*, *Materials Today: Proceedings*, 2018, **5**(1), 650–656.
- 26 Y. J. Lee, *J. Cryst. Growth*, 2004, **266**(4), 568–572.
- 27 A. Ahmed, A. Rys, N. Singh, J. Edgar and Z. Yu, *J. Electrochem. Soc.*, 1992, **139**(4), 1146–1151.
- 28 M. Morita, S. Isogai, K. Tsubouchi and N. Mikoshiba, *Appl. Phys. Lett.*, 1981, **38**(1), 50–52.
- 29 X.-H. Xu, H.-S. Wu, C.-J. Zhang and Z.-H. Jin, *Thin Solid Films*, 2001, **388**(1–2), 62–67.
- 30 A. C. Jones, C. R. Whitehouse and J. S. Roberts, *Chem. Vap. Deposition*, 1995, **1**(3), 65–74.
- 31 D. Riihelä, M. Ritala, R. Matero, M. Leskelä, J. Jokinen and P. Haussalo, *Chem. Vap. Deposition*, 1996, **2**(6), 277–283.
- 32 P. Kelly and R. Arnell, *Vacuum*, 2000, **56**(3), 159–172.
- 33 G. Thompson, P. Skeldon, X. Zhou, K. Shimizu, H. Habazaki and C. Smith, *Aircr. Eng.*, 2003, **75**(4), 372–379.
- 34 S. Kai Wang, H.-G. Liu and A. Toriumi, *Appl. Phys. Lett.*, 2012, **101**(6), 061907.
- 35 P. Motamedi and K. Cadien, *Appl. Surf. Sci.*, 2014, **315**, 104–109.
- 36 J.-J. Huang, L.-T. Huang, M.-C. Tsai, M.-H. Lee and M.-J. Chen, *Appl. Surf. Sci.*, 2014, **305**, 214–220.
- 37 C. Zhao, S. Taylor, M. Werner, P. Chalker, R. Murray, J. Gaskell, *et al.*, *J. Appl. Phys.*, 2009, **105**(4), 044102.
- 38 D. Vanderbilt, X. Zhao and D. Ceresoli, *Thin Solid Films*, 2005, **486**(1–2), 125–128.
- 39 J. Robertson, *Rep. Prog. Phys.*, 2005, **69**(2), 327.
- 40 S. Bang, S. Lee, S. Jeon, S. Kwon, W. Jeong, S. Kim, *et al.*, *J. Electrochem. Soc.*, 2008, **155**(9), H633–H637.
- 41 C. Scanlan, M. Gajdardziska-Josifovska and C. Aita, *Appl. Phys. Lett.*, 1994, **64**(26), 3548–3550.
- 42 Y.-H. Wu, L.-L. Chen, R.-J. Lyu, M.-Y. Li and H.-C. Wu, *IEEE Electron Device Lett.*, 2010, **31**(9), 1014–1016.
- 43 R. Hegde, D. Triyoso, S. Samavedam and B. White Jr, *J. Appl. Phys.*, 2007, **101**(7), 074113.



- 44 J. Robertson and R. M. Wallace, *Mater. Sci. Eng., R*, 2015, **88**, 1–41.
- 45 R. Engel-Herbert, Y. Hwang and S. Stemmer, *J. Appl. Phys.*, 2010, **108**(12), 124101.
- 46 E. H. Nicollian, J. R. Brews and E. H. Nicollian, *MOS (metal oxide semiconductor) physics and technology*, Wiley, New York, 1982.
- 47 K. Martens, C. O. Chui, G. Brammertz, B. De Jaeger, D. Kuzum, M. Meuris, *et al.*, *IEEE Trans. Electron Devices*, 2008, **55**(2), 547.
- 48 C.-C. Hsu, W.-C. Chi, Y.-H. Tsai, M.-L. Tsai, S.-Y. Wang, C.-H. Chou, *et al.*, *J. Vac. Sci. Technol., B*, 2018, **36**(5), 051204.
- 49 A. Nayfeh, C. O. Chui, K. C. Saraswat and T. Yonehara, *Appl. Phys. Lett.*, 2004, **85**(14), 2815–2817.
- 50 C.-M. Lin, H.-C. Chang, I.-H. Wong, S.-J. Luo, C. Liu and C. Hu, *Appl. Phys. Lett.*, 2013, **102**(23), 232906.
- 51 F. Ji, J. Xu, P. Lai, C. Li and J. Liu, *IEEE Electron Device Lett.*, 2011, **32**(2), 122–124.

